https://doi.org/10.1016/j.ijheatmasstransfer.2015.01.032
This is the Pre-Published Version.

Conjugate heat and mass transfer in a total heat exchanger with cross-corrugated triangular ducts and one-step made asymmetric membranes

Zhen-Xing Li[1], Ting-Shu Zhong[1], Jian-Lei Niu[2], Fu Xiao[2], Li-Zhi Zhang[1,3,*]

1. Key Laboratory of Enhanced Heat Transfer and Energy Conservation of Education Ministry, School of Chemistry and Chemical Engineering, South China University of Technology, Guangzhou 510640, China.
2. Dept. Building Services Engineering, the Hong Kong Polytechnic University, Hong Kong, China
3. State Key Laboratory of Subtropical Building Science, South China University of Technology, Guangzhou 510640, China.

Abstract

Membrane-based total heat exchanger is a device to recover both sensible heat and moisture from exhaust air stream from a building. Heat and mass transfer intensification has been undertaken by using a structure of cross-corrugated triangular ducts. To further intensify moisture transfer, recently developed membranes-one step made asymmetric membranes, are used as the exchanger materials. Conjugate heat and mass transfer under transitional flow regime in this total heat exchanger are investigated. Contrary to the traditional methods of assuming a uniform temperature (concentration) or a uniform heat flux (mass flux) boundary condition, in this study, the real boundary conditions on the exchanger surfaces are obtained by the numerical solution of the coupled equations that govern the transfer of momentum, energy and moisture in the two air streams and in the membrane materials. The naturally formed heat and mass boundary conditions are then used to calculate the local and mean Nusselt and Sherwood numbers along the exchanger ducts, in the heat and mass developing regions. The data are compared with those results under uniform temperature (concentration) and uniform heat flux (mass flux) boundary conditions, for cross-corrugated triangular ducts with typical duct apex angles of 60 and 90 degrees.

Keywords: Conjugate heat and mass transfer, cross-corrugated triangular ducts, total heat exchanger, asymmetric membrane

* Author for correspondence. Tel/fax: 86-20-87114264; Email: lzzhang@scut.edu.cn

© 2015. This manuscript version is made available under the CC-BY-NC-ND 4.0 license https://creativecommons.org/licenses/by-nc-nd/4.0/

Nomenclature

A_{cyc}	surface area of a flow cycle (m^2)
A_{ci}	cross-sectional area at inlet (m^2)
c_p	specific heat of fluid (kJ kg^{-1} K^{-1})
d_p	membrane pore diameter (μm)
D_h	hydrodynamic diameter (m)
D_{va}	moisture diffusivity in dry air (m^2/s)
D_{vm}	effective moisture diffusivity in membrane (m^2/s)
f	friction factor
H	changnel height (mm)
h	heat flux (kW/m^2)
h_{tot}	convective heat transfer coefficient (kW m^{-2} K^{-1})
k	turbulent kinetic energy (m^2/s^2)
k_{tot}	convective mass transfer coefficient (m/s)
m_v	moisture emission rate through membrane (kg m^{-2}·s^{-1})
Nu	Nusselt number
P	pressure (Pa)
q	mass diffusion flux (kg m^{-2} s^{-1})
Sc	Schmidt number
Sh	Sherwood number
Re	Reynolds number
T	temperature (K)
u	velocity (m/s)
V_a	air flow rate (m^3/s)
V_{cyc}	volume of a flow cycle (m^3)
W	channel width (mm)
Y_v	humidity ratio (kg/kg)
x, y, z	coordinates (m)

Greek letters

ρ	density (kg/m^3)
ν	kinematic viscosity (m^2/s)
λ	thermal conductivity (kW m^{-1} K^{-1})

μ	dynamic viscosity (Pa·s)
τ	shear stress (N/m^2)
ω	specific dissipation rate (s^{-1})
ε	turbulent dissipation rate (m^2/s^3)
δ	thickness of the membrane (m)
ψ	correction factor
θ	apex angle (°)
γ	orientation angle of neighboring layers (°)
φ	air leakage ratio

Superscripts

t	turbulent
′	fluctuation

Subscripts

a	air
c	conjugated
cyc	cyclic
e	exhaust air
f	fresh air
H	heat flux
i	inlet
J	mass flux
m	mean, membrane
o	outlet
T	temperature
v	vapor
W	wall, concentration

1. Introduction

Conditioning ventilation air typically constitutes 20% to 40% of the thermal load for commercial buildings and can be even higher in buildings that require 100% outdoor air to meet ventilation standards. It is well known that energy recovery devices could save a large fraction of the thermal load since heat and

humidity would be recovered from the exhaust stream in winter and excess heat and moisture would be transferred to the exhaust in order to cool and dehumidify the incoming air (fresh) in the summer. With energy recovery devices, the efficiency of existing HVAC systems can also be improved because otherwise fresh air needs to be dehumidified by cooling coil through condensation followed by a re-heating process, which is very energy intensive.

Membrane-based total heat exchanger has attracted much attention to fulfill this task [1-3]. The device is just like an air-to-air parallel plate sensible heat exchanger. But in place of traditional metal heat exchange plates, hydrophilic membranes, which can transfer both heat and moisture simultaneously, are used as the heat and mass transfer media. The device has many virtues like it is stationary, compact, and easy to construct. However, practical application until now is still scarce. The reason is that heat and mass transfer in the unit is slow, which limits their market penetrations.

To intensify heat and mass transfer, in this study, a novel duct structure, cross-corrugated triangular ducts, is used to augment heat and mass transfer in air side. The structure is shown in Fig.1. It has similar geometry as chevron plates used in traditionally heat exchangers (primary surface heat exchangers). But the cross section is triangular other than sinusoidal. Literature review found that though heat transfer [4-16] and mass transfer [17-19] in chevron plate heat exchangers have been investigated by various investigators, cross corrugated triangular ducts are less fully studied.

Fig.1.

Of the limited number of studies with this structure, the boundary conditions are assumed either as uniform temperature or uniform heat flux boundary conditions [20-24]. That assumption may hold for common metal heat exchangers. However, for a total heat exchanger, the heat and mass transfer in the ducts are closely coupled with the membranes. A uniform temperature or a uniform heat flux boundary condition is not justified. This is a conjugate heat mass transfer problem. To address this problem, in this study, the heat and mass transfer under real boundary conditions will be considered. This is a naturally formed boundary condition resulted from the interactions between the two flows, and the membrane.

Further, besides air side augmentation, material side augmentation is also undertaken. A novel kind of membrane developed recently [25], the so called one-step made asymmetric membrane, is used as the exchanger material. The membranes are made from CA, Cellulose Acetate. The benefit with this material is that it is simple in fabrication processes. So it is cheap. However the moisture permeability through this membrane is 1.5-2 times higher than previously developed membranes [26].

2. Experimental works

A test rig is built to perform heat mass transfer and pressure drop experiments, as shown in Fig.2. It comprises of variable speed blowers, wind tunnels, heaters, humidifiers, nozzles and the total heat exchanger core. Air in one side is conditioned to simulate the outdoor fresh air. The other side is to simulate the indoor stale air. The volumetric air flow rates can be adjusted to have different Reynolds numbers. The low speed wind tunnels are to ensure a continuous, steady air supply. The volumetric air flow rates are measured by a set of nozzles in the wind tunnel. Temperature and humidity sensors are inserted into the test section to measure the states of inlet and outlet air.

The leakage between the two streams mainly occurs in the joining parts the core and the supporting frames. To check the air leakage rate, air flow rates are tested in the test section by measuring area-averaged air velocities. Nine test points are uniformly distributed in the wind channel. The air leakage rate in each side is calculated by

$$\varphi = \frac{V_{\mathrm{i}} - V_{\mathrm{o}}}{V_{\mathrm{i}}} \times 100\% \tag{1}$$

where V is air volumetric flow rate (m^3/s), subscript i and o represents inlet and outlet. It is less than 5% in this work. Only the air leakage rate is assured, can the experiment be executed.

Fig.2.

A total heat exchanger core with cross corrugated triangular ducts is assembled, as depicted in Fig.3. One-step made asymmetric CA membranes are used as the exchanger material. The detailed fabrication processes have been introduced in [25]. This kind of novel membranes is simple in making processes, so they are cheap. The moisture permeability is 1.5-2 times higher than traditional vapor permeable membranes, because asymmetric finger-like macrovoids are generated during the coagulation exchange process. These finger-like macrovoids can sharply decrease the moisture diffusion resistance. A skin layer is formed on the membrane surface in one-step before the coagulation process, which ensures better selectivity and high moisture permeability. With the new membranes, material side heat mass transfer augmentation is realized.

Fig.3.

After the membranes are made, the flat membrane sheets are corrugated to form a series of parallel equilateral triangular ducts, with apex angles of 90 degrees. Sheets of the corrugated plates are then stacked together to form a 90 degree orientation angle γ between the neighboring plates, which guarantees the same flow pattern for both fluids. The channel height H is 7 mm, and channel width W is 14mm. The

membrane thickness is kept constant during manufacturing. The membranes are very thin and soft, which requires plastic frame cases to support them. Consequently, with a pre-designed plastic frame, triangular duct walls are formed to construct the required geometry. The structure gives better air side heat mass transfer capabilities. This efficiency improvement is attributed to the pattern of flow that undergoes abrupt turnaround, contraction, and expansion. The physical properties of the membranes are given in Table 1.

Table 1.

Inlet and outlet air states are measured under different air flow rates. The thermal properties of air are assumed to be constant, because the temperature difference between indoor air and outdoor air is less than 10 K. The pressure drop, Nusselt and Sherwood numbers are then calculated with the measured inlet and outlet air states. Energy and mass balances between two sides of membranes are checked to be within 1%.

The sensible effectiveness is calculated as

$$\varepsilon_{\mathrm{s}} = \frac{m_{\mathrm{f}}(T_{\mathrm{fi}} - T_{\mathrm{fo}}) + m_{\mathrm{e}}(T_{\mathrm{eo}} - T_{\mathrm{ei}})}{2m_{\min}(T_{\mathrm{fi}} - T_{\mathrm{ei}})} \tag{2}$$

where m_{f} and m_{e} are the mass flow rate of fresh air and exhaust air, respectively. $m_{\min}$ is the least one of m_{f} and m_{e}. T is the temperature of air. The subscripts ‘f, e, i, e’ mean fresh air, exhaust air, inlet and outlet, respectively. In the experiment, flow rates of fresh air and exhaust air are equal. So Eq.(2) can be simplified as

$$\varepsilon_{\mathrm{s}} = \frac{(T_{\mathrm{fi}} - T_{\mathrm{fo}}) + (T_{\mathrm{eo}} - T_{\mathrm{ei}})}{2(T_{\mathrm{fi}} - T_{\mathrm{ei}})} \tag{3}$$

The latent effectiveness is calculated as

$$\varepsilon_{\mathrm{L}} = \frac{(Y_{\mathrm{fi}} - Y_{\mathrm{fo}}) + (Y_{\mathrm{eo}} - Y_{\mathrm{ei}})}{2(Y_{\mathrm{fi}} - Y_{\mathrm{ei}})} \tag{4}$$

where Y represents humidity ratio in fresh air or exhaust air side.

With the measured inlet and outlet mean variables, the heat transfer coefficient can be calculated by

$$h_{\mathrm{tot}} = \frac{c_{\mathrm{pa}}\rho_{\mathrm{a}}V_{\mathrm{a}}((T_{\mathrm{fi}} - T_{\mathrm{fo}}) + (T_{\mathrm{ei}} - T_{\mathrm{eo}}))}{2A_{\mathrm{tot}}\Delta T_{\mathrm{m}}} \tag{5}$$

and

$$\Delta T_{\mathrm{m}} = \psi \frac{(T_{\mathrm{fi}} - T_{\mathrm{eo}}) - (T_{\mathrm{fo}} - T_{\mathrm{ei}})}{\ln \frac{T_{\mathrm{fi}} - T_{\mathrm{eo}}}{T_{\mathrm{fo}} - T_{\mathrm{ei}}}} \tag{6}$$

where c_{pa} is specific heat of air, ρ_a is density of the air (kg/m^3), V_a is the air flow rate of fresh air or exhaust air (m^3/s). A_{tot} is the total surface area of membrane (m^2). ΔT_m is the log mean temperature difference. ψ is a correction factor for cross flow [27], and it is about 0.96 in this study.

The Nusselt number is calculated by

$$Nu = \frac{h_f D_h}{\lambda_a} \tag{7}$$

where λ_a is air thermal conductivity (kW m^{-1} K^{-1}), h_f is the convective heat transfer coefficient in fresh air side (kW m^{-2} K^{-1}), and can be derived from

$$\frac{1}{h_{tot}} = \frac{1}{h_f} + \frac{\delta}{\lambda_{mem}} + \frac{1}{h_e} \tag{8}$$

where δ is membrane thickness (m), λ_{mem} is thermal conductivity of the membrane (kW m^{-1} K^{-1}). h_e is the convective heat transfer coefficient in exhaust air side, and nearly equals to h_f.

The mass transfer coefficient can be calculated by

$$k_{tot} = \frac{\rho_a V_a ((Y_{fi} - Y_{fo}) + (Y_{ei} - Y_{eo}))}{2 A_{tot} \Delta Y_v} \tag{9}$$

where ΔY_v is the log mean humidity difference, and

$$\Delta Y_v = \psi \frac{(Y_{fi} - Y_{eo}) - (Y_{fo} - Y_{ei})}{\ln \frac{Y_{fi} - Y_{eo}}{Y_{fo} - Y_{ei}}} \tag{10}$$

The Sherwood number is calculated by

$$Sh = \frac{k_f D_h}{D_{va}} \tag{11}$$

where D_{va} is moisture diffusion in air (m^2/s), k_f is the convective mass transfer coefficient in fresh air side (m/ s), and can be derived from

$$\frac{1}{k_{tot}} = \frac{1}{k_f} + \frac{\delta}{D_{vm}} + \frac{1}{k_e} \tag{12}$$

where D_{vm} can be measured using the field and laboratory emission cell (FLEC) [28]. k_e is the convective mass transfer coefficient in exhaust air side (m/ s), and it nearly equals to k_f. With above equation, the membrane side resistance is subtracted and the air side coefficient is obtained.

The friction factor is calculated by

$$f = \frac{(P_i - P_o) D_h}{\frac{1}{2} \rho_a u_m^2 x_F} \tag{13}$$

where x_F is the length of the core, (m); P_i and P_o are pressure at inlet and outlet of the core, respectively, (Pa).

The hydraulic diameter of the exchanger channel is defined as

$$D_h = \frac{4V_{cyc}}{A_{cyc}} \tag{14}$$

where V_{cyc} and A_{cyc} are the volume and the surface area of a cycle in the channel, which has been shown in Fig.1.

The uncertainties for measurement are: temperature, ±0.2℃; humidity, ±2%; volumetric flow rate, ±0.5%; pressure drop, ±1 Pa; velocity, ±2.5%，the final uncertainties for friction factor is 9.2%, for sensible efficiency is 4.2%, for humidification efficiency is 6.7%, for heat transfer coefficient is 4.6%, for mass transfer coefficient is 5.3%.

3. Numerical method and equations

3.1. Governing Equations

Traditionally, heat mass transfer in total heat exchanger ducts is modeled by assuming a uniform temperature or uniform heat flux boundary conditions on membrane surfaces. Convective heat transfer coefficients are calculated under these ideal boundary conditions. Then the Chilton–Colburn *j* factor analogy is used to estimate mass transfer coefficients from the previously calculated heat transfer coefficients. However recent studies found that for these large-Biot number ducts like membrane formed ducts, the traditional Chilton–Colburn *j* factor analogy fails due to very different heat and mass transfer boundary conditions on duct surfaces [29]. The membrane should be investigated together with adjacent air streams. It is in nature a conjugate problem. Therefore in this study, the membrane material and the neighboring two streams are modeled together, because of the close interactions between the air streams and the membrane material. The exchanger has 67 layers of membranes, which form 33 channels for each stream. Direct modeling of every channel is very time consuming. So only a section in the middle of the exchanger is selected as the calculating domain. It comprises of 7 layers of neighboring ducts. These 7 layers of membranes form 4 ducts for fresh air and 3 ducts for exhaust air. The change of thermal properties with temperature is ignored, because the temperature difference between indoor air and outdoor air is small.

The general form of the mass continuity equation in the duct is shown below as

$$\frac{\partial \rho u_j}{\partial x_j} = 0 \tag{15}$$

where ρ is the fluid density (kg/m^3), u is flow velocity (m/s).

Flow in the cross corrugated triangular ducts are mostly in transitional flow regime, even under very low Reynolds numbers due to disturbances from the corrugations. A low Reynolds number k-ω model is

employed in this investigation as the model has been previously validated in [24] to grasp the transitional flow behaviors in the channel. The Navier-Stokes equations in the ducts is

$$\frac{\partial}{\partial x_j}(\rho u_i u_j) = -\frac{\partial P}{\partial x_i} + \frac{\partial}{\partial x_j}(\tau_{ij} + \tau_{ij}^t) \tag{16}$$

$$\tau_{ij} = \mu(\frac{\partial u_i}{\partial x_j} + \frac{\partial u_j}{\partial x_i}); \qquad \tau_{ij}^t = -\rho\overline{u_i' u_j'} \tag{17}$$

where P and μ are pressure (Pa) and dynamic viscosity (Pa·s), respectively.

The energy equation is

$$\frac{\partial}{\partial x_j}(\rho c_p u_j T) = \frac{\partial}{\partial x_j}(h_j + h_j^t) \tag{18}$$

where

$$h_j = \frac{\mu c_p}{\mathrm{Pr}}\frac{\partial T}{\partial x_j}; \qquad h_j^t = -\rho c_p \overline{u_j' T'} \tag{19}$$

where λ is the thermal conductivity (kW m^{-1} K^{-1}).

The equation for moisture mass conversation is

$$\frac{\partial}{\partial x_j}(\rho u_j Y_v) = \frac{\partial}{\partial x_j}(q_j + q_j^t) \tag{20}$$

$$q_j = D_{va}\frac{\partial Y_v}{\partial x_j}; \qquad q_j^t = -\rho\overline{u_j' Y_v'} \tag{21}$$

D_{va} is the moisture diffusivity in dry air (m^2/s).

The turbulent shear stress is determined by

$$\tau_{ij}^t = \mu_t(\frac{\partial u_i}{\partial x_j} + \frac{\partial u_j}{\partial x_i}) - \frac{2}{3}\delta_{ij} k\rho \tag{22}$$

where δ_{ij} is the Kronecker delta function, δ_{ij} = 1 when $i = j$ and zero when $i \neq j$.

On solid boundaries, k should be zero and ω can be specified at the first few grid points away from the wall as

$$\omega = \frac{6\mu}{\beta y^2} \tag{23}$$

where y is the distance to wall. The resulting equations for k, ω, and ν_t are:

$$\nu_t = \frac{\mu_t}{\rho} = \alpha^* \frac{k}{\omega} \tag{24}$$

The equations for k and ω are described as

$$u_j \frac{\partial k}{\partial x_j} = \tau_{ij} \frac{\partial u_i}{\partial x_j} - \beta^* \omega k + \frac{\partial}{\partial x_j}[(\nu + \sigma_k \nu_t) \frac{\partial k}{\partial x_j}] \tag{25}$$

$$u_j \frac{\partial \omega}{\partial x_j} = \frac{\sigma}{\nu_t} \tau_{ij} \frac{\partial u_i}{\partial x_j} - \beta_2 \omega^2 + \frac{\partial}{\partial x_j}[(\nu + \sigma_\omega \nu_t) \frac{\partial \omega}{\partial x_j}] + 2\sigma_{\omega 2} \frac{1}{\omega} \frac{\partial k}{\partial x_j} \frac{\partial \omega}{\partial x_j} \tag{26}$$

The model constants are provided in Refs [30, 31]:

$$\beta^* = \frac{9}{100} \frac{\frac{5}{18} + \left(\frac{\mathrm{Re_t}}{R_\beta}\right)^4}{1 + \left(\frac{\mathrm{Re_t}}{R_\beta}\right)^4} \tag{27}$$

$$\alpha^* = \frac{\alpha_0^* + \frac{\mathrm{Re_t}}{R_k}}{1 + \frac{\mathrm{Re_t}}{R_k}} \tag{28}$$

$$\alpha = \frac{5}{9} \frac{\alpha_0 + \frac{\mathrm{Re_t}}{R_\omega}}{1 + \frac{\mathrm{Re_t}}{R_\omega}} (\alpha^*)^{-1} \tag{29}$$

$$\mathrm{Re_t} = \frac{\rho k}{\mu \omega} \tag{30}$$

$$\beta_2 = 0.078 \frac{1 + 85\chi_\omega}{1 + 100\chi_\omega} \tag{31}$$

$$\chi_\omega = \left| \frac{\Omega_{ij} \Omega_{jk} S_{ki}}{(0.09\omega)^3} \right| \tag{32}$$

$$\Omega_{ij} = \frac{1}{2}\left(\frac{\partial u_i}{\partial x_j} - \frac{\partial u_j}{\partial x_i} \right) \tag{33}$$

$$S_{ij} = \frac{1}{2}\left(\frac{\partial u_i}{\partial x_j} + \frac{\partial u_j}{\partial x_i} \right) \tag{34}$$

Other empirical constants in the equations are

β=0.075, α_0=0.1, σ_k=0.5, σ_ω=0.5, R_β=0.8, R_k=0.6, α_0^*=β/3, R_ω=2.7, σ=0.52, $\sigma_{\omega 2}$=0.75

The turbulent heat transfer term in Eq. (19) is determined by the following equation

$$h_j^t = \frac{\mu_t}{\sigma_\theta} \frac{\partial T}{\partial x_j} \tag{35}$$

where the empirical constant takes σ_θ=1.3 [24].

The mass transfer is combined with k-ω equations through Eq. (21) in the form of

$$q_j^{\mathrm{t}} = \frac{\mu_{\mathrm{t}}}{Sc_{\mathrm{t}}} \frac{\partial Y_{\mathrm{v}}}{\partial x_j} \tag{36}$$

The empirical constant turbulent Schmidt number takes 0.7 [32, 33].

The Reynolds number, Re, is

$$\mathrm{Re} = \frac{\rho_{\mathrm{a}} u_{\mathrm{m}} D_{\mathrm{h}}}{\mu_{\mathrm{a}}} \tag{37}$$

where u_{m} is the area-weighted mean velocity at the inlet (m/s).

Convective heat transfer coefficient in fresh air side is calculated by

$$h_{\mathrm{f}} = \frac{c_{\mathrm{pa}} \rho_{\mathrm{a}} u_{\mathrm{m}} A_{\mathrm{ci}} (T_{\mathrm{fi}} - T_{\mathrm{fo}})}{A_{\mathrm{cyc}} \Delta T_{\mathrm{m}}} \tag{38}$$

where A_{ci} is the cross-sectional area at inlet or outlet of a cycle (m^2); A_{cyc} is the surface area of the channel (m^2); ΔT_{m} is the logarithmic temperature difference between the membrane and the fluid, which is calculated by

$$\Delta T_{\mathrm{m}} = \psi \frac{(T_{\mathrm{fi}} - T_{\mathrm{wi}}) - (T_{\mathrm{ei}} - T_{\mathrm{wo}})}{\ln \dfrac{T_{\mathrm{fi}} - T_{\mathrm{wi}}}{T_{\mathrm{ei}} - T_{\mathrm{wo}}}} \tag{39}$$

Convective mass transfer coefficient is calculated by

$$k_{\mathrm{f}} = \frac{\rho_{\mathrm{a}} u_{\mathrm{m}} A_{\mathrm{ci}} (Y_{\mathrm{fi}} - Y_{\mathrm{fo}})}{A_{\mathrm{cyc}} \Delta Y_{\mathrm{v}}} \tag{40}$$

and

$$\Delta Y_{\mathrm{v}} = \psi \frac{(Y_{\mathrm{fi}} - Y_{\mathrm{wi}}) - (Y_{\mathrm{ei}} - Y_{\mathrm{wo}})}{\ln \dfrac{Y_{\mathrm{fi}} - Y_{\mathrm{wi}}}{Y_{\mathrm{ei}} - Y_{\mathrm{wo}}}} \tag{41}$$

Then Nu and *Sh* can be obtained through Eqs. (7) and (11).

3.2 Solution method

A non-staggered mesh structure is used, and the size near wall is smaller than in duct. The meshes on the outside walls of a computational block are shown in Fig.4. The graph only depicts a part of the adoptive meshes, to get an amplified view of the mesh structure. Totally there are 10 cycles in *x* and *z* direction, and 7 layers in *y* direction.

Fig.4.

Boundary conditions are defined. Non-slip velocity wall conditions are assumed. In the interior of the core, the fresh air and exhaust air exchange moisture through the membrane. Thus the temperature and humidity on membrane surfaces are neither uniform values nor uniform fluxes. That means the temperature and humidity vary along the membrane surfaces. The membrane thickness is kept constant in the preparation process. Due to the small thickness in membrane (100 μm, thermal conductivity 0.127 W/(m · K), temperature differences between the two sides of a membrane are rather small. Thus for heat transfer condition, on the two sides of the membrane at the same point, there has

$$\left.\frac{\partial T_{\mathrm{f}}}{\partial n}\right|_{(x,y,z)=(x_{\mathrm{m1}},y_{\mathrm{m1}},z_{\mathrm{m1}})}=\left.\frac{\partial T_{\mathrm{e}}}{\partial n}\right|_{(x,y,z)=(x_{\mathrm{m2}},y_{\mathrm{m2}},z_{\mathrm{m2}})} \tag{42}$$

For mass transfer condition, on the two sides of membrane at the same point, there has

$$m_{\mathrm{v}}=\rho_{\mathrm{m}}D_{\mathrm{vm}}\left(\frac{Y_{\mathrm{vf}}-Y_{\mathrm{ve}}}{\delta}\right)=-\rho_{\mathrm{a}}D_{\mathrm{va}}\left.\frac{\partial Y_{\mathrm{vf}}}{\partial n}\right|_{(x,y,z)=(x_{\mathrm{m1}},y_{\mathrm{m1}},z_{\mathrm{m1}})}=-\rho_{\mathrm{a}}D_{\mathrm{va}}\left.\frac{\partial Y_{\mathrm{ve}}}{\partial n}\right|_{(x,y,z)=(x_{\mathrm{m2}},y_{\mathrm{m2}},z_{\mathrm{m2}})} \tag{43}$$

where m_{v} (kg/(m^{2}s))) is the moisture emission rate through membrane. ρ_{m} and D_{vm} are density of membrane and moisture diffusivity in membrane, respectively. δ is the thickness of the membrane(m). Subscript ‘‘m” refers to membrane, and ‘‘1” and ‘‘2” refer to fresh side and exhaust side at the same point of membrane, respectively.

For the top layer and the bottom layer membranes in the exchanger section, zero heat and mass flux boundary conditions (adiabatic) are assumed. In the interior, the boundary conditions on membranes are naturally formed by the coupling between the fresh air and the exhaust air. A real exchanger usually has more than 100 layers of membranes, which is difficult to simulate directly, on a channel-to-channel basis. So only a section of several neighboring channels are simulated. The boundary conditions on the top and the bottom layer membranes of this section would affect the calculation accuracy. To minimize this effect, 7 layers of flow channels are selected for calculation but only the channel in the center (the fourth flow channel) is used for overall mean Nusselt and Sherwood numbers (Nu_{m} and Sh_{m}) calculations. The larger the number of calculated layers are, the less the effects from the top and bottom layers are. The differences of Nu_{m} and Sh_{m} between a 7-layers domain and a 8-layers domain are less than 1%, as shown in Fig.5. Therefore the 7 layers domain is assumed enough and is selected. At the inlet, velocity is set to uniform and normal to the inlet face. The inlet humidity ratio in fresh air and exhaust air are set to 0.024kg/kg and 0.011kg/kg respectively. The inlet temperatures for fresh air and exhaust air are 308K and 300K respectively. The boundary condition for outlet is defined as

$$\frac{\partial \phi}{\partial n}=0 \tag{44}$$

where ϕ represents the calculated variable, n means normal direction of the outlet face.

Fig.5.

The governing equations are solved by using standard finite difference methods that employ control-volume based discretization techniques along with a pressure-correction algorithm. The N-S equations are solved by SIMPLEC scheme, while the convective and diffusive terms in the energy equation are solved by QUICK scheme, which has second-order accuracy.

The grid independency test has been done. The calculations were primarily carried out with three different grid densities, 469985, 626470, and 1454169 mesh points. The channel fully developed periodic mean pressure drop and temperature change with the two finer grids are within 1% differences and 14% lower than those with the coarse grid. For the finest grids, 1454169, the solution time is very long, which is hard to use practically. Based on the above grid independency tests, the final calculations are performed with the 626470 grids and the results obtained in this paper refer to the grid geometry mentioned above.

4. Results and discussions

4.1 Model validation

Experimental work is used to validate the model and the methodology. The core's apex angle is 90 degrees. Both volumetric air flow rates and inlet air conditions are changed in the experiment. Outlet air parameters under different operating conditions are measured and calculated. The test data are then compared with the calculated data, as shown in Table 2. The outlet parameters are compared. The resulting sensible and latent effectiveness, as well as the friction factors are also compared. Generally, the maximum difference between the numerical and tested temperatures is below 2%. The maximum difference for humidity is below 3.5%. The maximum difference for pressure drops is 11%. The maximum difference for sensible effectiveness, latent effectiveness, and friction factor, are 10.5%, 5.8% and 10.7%. From this analysis the model and the methodology are verified.

Table 2.

4.2 Flow distribution

Fig.6 shows the velocity contours in the *x-y* plane at the center of *x* axis, for Re=890. As seen from this figure, the flow has two distinct patterns: in the corrugation troughs of the upper wall, the flow is parallel steady flow, while in the troughs of the lower wall, fluid re-circulation or swirl flows are generated due to the reason that the fluid separates from the rear-facing facet and reattaches to the front facing facet. The

shapes of flow re-circulation in the valleys become almost identical to each other, after 3-5 cycles, indicating a cyclic manner. The maximum value of the velocity occurs near the peaks of the lower wall, where the flow has the least cross sectional area. The velocity is the smallest where the duct expansion occurs. The vortexes resulted from duct expansion and contraction are helpful for momentum transfer. The apex angle has effect on flow distribution in the flow channel. The vortexes in the 60 degrees case are more obvious than in 90 degree case. The temperature gradient is also larger in the 60 degrees flow channel. As can be deducted, when the apex angle is larger, the cross-corrugated flow channel is more similar to parallel plate duct. That means the turbulent motion will be depressed as the flow channel became flatten. So the heat and mass transfer will decrease when the apex angle decreases.

Fig.6.

4.3 Temperature distribution and Nusselt numbers

The temperature contours shown in Fig.7 in a *y*-*z* mid-plane for Re=890 clearly show a cyclic manner. After 4-6 cycles, the heat boundary layer has become fully developed. In the corrugation troughs of the upper wall, parallel flow is predominant, while in the troughs of the lower wall, clock-wise strong swirls are generated due to the fact that the fluid turns abruptly when facing the trough walls of the lower wall. Flow conditions also have an influence on temperature distribution. At smaller Re numbers, temperature gradients in the valleys of the lower wall are smaller, due to the reduced intensities of swirls. Fig.8 shows the isotherms and heat fluxes on the membrane surface in the middle layer. It is clear that the boundary conditions on the membrane surface are neither uniform temperature nor uniform heat flux. The temperature contours vary along both *x* and *z* directions. The temperature in the fresh air side and exhaust air side is coupled through the membrane.

Fig.9 shows the mean Nusselt numbers for each cycle, Nu_{cyc} under different flow rates. At the entrance, the cyclic mean Nusselt numbers are very high, due to very thin boundary layers at the entrance. Along the flow direction, the cyclic mean Nusselt numbers decrease rapidly in the first 4-6 cycles, and then arrive gradually at some stable values. They are denoted as the fully developed values, Nu_C. If the boundary conditions are under uniform temperature, they are Nu_T. If the boundary conditions are under uniform heat flux, they are Nu_H.

The detailed values of Nu_C are shown in Fig.10. For comparison, the values of Nu_T and Nu_H are also listed. When the apex angle is 60 degrees, Nu_C is only about 57-64% of Nu_T, and 52-55% of Nu_H. Because under the real conjugated boundary conditions, the mean temperature on the membrane surface is less than that under ideal uniform temperature or uniform heat flux boundary conditions, heat transfer is

deteriorated by these "imperfect" boundary conditions. So the Nusselt numbers drop. The heat transfer coefficients are also influenced by apex angle of the duct. The higher the apex angle is, the less the effects of flow maldistribution are, and the higher the heat transfer coefficients are. When the flow channel is more flattened, say, with an angle of 90 degrees, the trend of Nu_C is between Nu_T and Nu_H. This is because boundary values on the membrane surfaces are more homogeneous. When the channel is more sharp, with an angle of 60 degrees, Nu_C even lower than Nu_T. This is because boundary values on membrane surfaces are rather inhomogeneous, which makes real heat and mass transfer capabilities low. Similar conclusions can be seen in Zhang [22, 34] and Huang et al. [35].

Fig.7.

Fig.8.

Fig.9.

Fig.10.

4.4 Sherwood Numbers

Fig.11 shows the contour profiles of humidity ratio on a *y*-*z* plane at the center of *x* axis for Re=890. Fig.12 shows the humidity ratios on the membrane surface in the middle layer (fresh air side). The humidity ratio contours in the cross-corrugated ducts have similar distributions as temperature contours. The detailed values of Sh_C for apex angles of 60 and 90 degrees are shown in Fig.13. Test data are also drawn. The values of Sh_w (uniform mass concentration) and Sh_J (uniform mass flux) are also plotted for comparison. The duct aspect ratio also has similar influences as on heat transfer. As seen from the graph, Sh_C is about 54-60% of Sh_W and 49-54% of Sh_J when apex angle is 60 degree. This is because the channel is more sharp and flow is more non-uniform. When the apex angle is 90 degrees, Sh_C is lower than Sh_W at low Res; but it gradually exceeds Sh_W as Re increases. This is because boundary values on the membrane surfaces are more homogeneous. When the Reynolds number increases, air side Nusselt and Sherwood numbers increase with augmented air side heat and mass transfer. The adverse effects of "imperfect" boundary conditions become less influential. The Sherwood numbers increase.

Fig.11.

Fig.12.

Fig.13.

4.5 Comparisons with parallel-plate and plate-fin structures and other membranes

Besides cross-corrugated triangular ducts, parallel-plates and plate-fin structures are also common structures for total heat exchangers. The three structures are compared here. Table 3 lists the heat and mass transfer properties of total heat exchangers with the three different core structures and different membranes. These data are calculated based on the same design conditions for the three cores: the same exchanger dimensions, the same membrane areas packed, and the same air flow rates. So the channel geometries are different from previously tested exchangers. The transport properties for the parallel-plate and plate-fin structure are taken from [29] and the transport data for the composite membrane are taken from [36]. As seen, the cross-corrugated structure intensifies air side convective heat and mass transfer substantially. Further, the heat and moisture resistance in the asymmetric membranes is smaller than in composite membranes. These two factors make the new total heat exchanger more efficient and have higher heat mass transfer capabilities. The cross corrugated triangular duct structure with asymmetric membranes has a sensible effectiveness of 0.86, and a latent effectiveness of 0.81. In contrast, the plate-fin structure with composite membranes has a sensible effectiveness of 0.55, and a latent effectiveness of 0.30. As a penalty, the pressure drop increased dramatically.

Table 3.

5. Conclusions

Conjugate heat and mass transfer in a total heat exchanger, which uses cross corrugated triangular duct structure and one-step made asymmetric membranes to augment both air side and material side heat and mass transfer, is investigated here. Through experimental and numerical analysis, following results can be found:

(1) For the cross-corrugated triangular ducts, both the flow and the heat and mass transfer demonstrate cyclic patterns. At the entrance region, the cyclicly mean values of friction factor, Nusselt and Sherwood numbers decrease rapidly along the flow. After 3-6 cycles, both the fluid flow and heat and mass transfer become fully developed. After the entry regions, the cyclic mean friction factors, Nusselt and Sherwood numbers come to stable values.

(2) The conjugated boundary conditions are neither uniform temperature (humidity) nor uniform heat flux (mass flux) boundary conditions. These “imperfect” boundary conditions have adverse effects on the Nusselt and Sherwood numbers, which are generally lower than the values under ideal conditions. When the apex angles of the ducts are larger, the Nusselt and Sherwoood numbers increase due to augmented air side heat and mass transfer and reduced adverse effects from conjugated boundary conditions.

(3) Compared to parallel-plate or plate-fin structures with common composite membrane materials, the cross-corrugated structure with one-step made asymmetric membranes would have a 20% higher sensible effectiveness, a 40% higher latent effectiveness, with about 4 times higher pressure drop penalty.

Acknowledgments

The Project is jointly supported by Natural Science Foundation of China No. 51161160562 and Research Grant Council of Hong Kong SAR Government No. N_PolyU513/11, under NSFC-RGC joint funding scheme.

References

[1] L.Z. Zhang, Y. Jiang, Heat and mass transfer in a membrane-based Enthalpy Recovery Ventilator, Journal of Membrane Science 163 (1999) 29-38.

[2] K.R. Kistler, E.L. Cussler, Membrane modules for building ventilation, Chemical Engineering Research & Design 80 (2002) 53-64.

[3] L.Z. Zhang, J.L. Niu, Effectiveness correlations for heat and moisture transfer processes in an enthalpy exchanger with membrane cores, ASME Journal of Heat Transfer 122 (2002) 922-929.

[4] W.W. Focke, J. Zachariades, I. Olivier, The effect of the corrugation inclination angle on the thermohydraulic performance of plate heat exchangers, International Journal of Heat and Mass Transfer 28 (1985) 1469-1479.

[5] M. Ciofalo, J. Stasiek, M.W. Collins, Investigation of flow and heat transfer in corrugated passages-II. Numerical simulations, International Journal of Heat and Mass Transfer 39 (1996) 165-192.

[6] S. Ergin, A. Ota, H. Yamaguchi, Numerical study of periodic turbulent flow through a corrugated duct, Numerical Heat Transfer,Part A: Applications 40 (2001) 139-156.

[7] J. Stasiek, M. Ciofalo, I.K. Smith, M.W. Collins, Investigation of flow and heat transfer in corrugated passages-I Experimental results, International Journal of Heat Mass Transfer 39 (1996) 149-192.

[8] H. Biomerius, C. Hoisken, N.K. Mitra, Numerical investigation of flow field and heat transfer in cross-corrugated ducts, ASME Journal of Heat Transfer 121 (1999) 314-321.

[9] S. Freund, S. Kabelac, Investigation of local heat transfer coefficients in plate heat exchangers with temperature oscillation IR thermography and CFD, International Journal of Heat and Mass Transfer 53 (2010) 3764-3781.

[10] X.H. Han, L.Q. Cui, S.J. Chen, G.M. Chen, Q. Wang, A numerical and experimental study of chevron, corrugated-plate heat exchangers, International Communications in Heat and Mass Transfer 37 (2010) 1008-1014.

[11] Z.Y. Liu, H.Y. Wu, Steady-State and Transient Investigation of the Primary Surface Recuperator for Microturbines, Heat Transfer Engineering 34 (2013) 875-886.

[12] J.A. Stasiek, Experimental studies of heat transfer and fluid flow across corrugated-undulated heat exchanger surfaces, International Journal of Heat and Mass Transfer 41 (1998) 899-914.

[13] Y.C. Tsai, F.B. Liu, P.T. Shen, Investigations of the pressure drop and flow distribution in a chevron-type plate heat exchanger, International Communications in Heat and Mass Transfer 36 (2009) 574-578.
[14] Q.W. Wang, D.J. Zhang, G.N. Xie, Experimental Study and Genetic-Algorithm-Based Correlation on Pressure Drop and Heat Transfer Performances of a Cross-Corrugated Primary Surface Heat Exchanger, Journal of Heat Transfer 131 (2009) 061802.
[15] L. Zhang, D.F. Che, Influence of Corrugation Profile on the Thermalhydraulic Performance of Cross-Corrugated Plates, Numerical Heat Transfer, Part A: Applications 59 (2011) 267-296.
[16] L.Z. Zhang, S.M. Huang, Coupled heat and mass transfer in a counter flow hollow fiber membrane module for air humidification, International Journal of Heat and Mass Transfer 54 (2011) 1055-1063.
[17] N. Tzanetakis, K. Scott, W.M. Taama, R.J.J. Jachuck, Mass transfer characteristics of corrugated surfaces, Applied Thermal Engineering 24 (2004) 1865-1875.
[18] D.W. Hall, K. Scott, R.J.J. Jachuck, Determination of mass transfer coefficient of a cross-corrugated membrane reactor by the limiting-current technique, International Journal of Heat and Mass Transfer 44 (2001) 2201-2207.
[19] K. Scott, J. Lobato, Mass Transport in Cross-Corrugated Membranes and the Influence of TiO_2 for Separation Processes, Industrial & Engineering Chemistry Research 42 (2003) 5697-5701.
[20] L.Z. Zhang, Turbulent Three-Dimensional Air Flow and Heat Transfer in a Cross-Corrugated Triangular Duct, Journal of Heat Transfer 127 (2005) 1151.
[21] L.Z. Zhang, Numerical Study of Periodically Fully Developed Flow and Heat Transfer in Cross-Corrugated Triangular Channels in Transitional Flow Regime, Numerical Heat Transfer, Part A: Applications 48 (2005) 387-405.
[22] L.Z. Zhang, Heat and mass transfer in a cross-flow membrane-based enthalpy exchanger under naturally formed boundary conditions, International Journal of Heat and Mass Transfer 50 (2007) 151-162.
[23] L.Z. Zhang, Laminar flow and heat transfer in plate-fin triangular ducts in thermally developing entry region, International Journal of Heat and Mass Transfer 50 (2007) 1637-1640.
[24] L.Z. Zhang, Z.Y. Chen, Convective heat transfer in cross-corrugated triangular ducts under uniform heat flux boundary conditions, International Journal of Heat and Mass Transfer 54 (2011) 597-605.
[25] X.R. Zhang, L.Z. zhang, H.M. Liu, L.X. Pei, One-step fabrication and analysis of an asymmetric cellulose acetate membrane for heat and moisture recovery, Journal of Membrane Science 366 (2011) 158-165.
[26] L.Z. Zhang, Progress on heat and moisture recovery with membranes: from fundamentals to engineering applications, Energy Conversion and Management 63 (2012) 173-195.
[27] T.L. Bergman, A.S. Lavine, F.P. Incropera, D.P. Dewitt, Introduction to Heat Transfer, John Wiley & Sons, Inc, 2011.
[28] L.Z. Zhang, J.L. Niu, Laminar fluid flow and mass transfer in a standard field and laboratory emission cell, International Journal of Heat and Mass Transfer 46 (2003) 91-100.
[29] L.Z. Zhang, Conjugate Heat and Mass Transfer in Heat Mass Exchanger Ducts, 1st ed., Academic Press, New York, 2013.
[30] R.M. Jones, A.D. Harvey, S. Acharya, Two equation turbulence modeling for impeller stirred tanks, Journal of Fluids Engineering 123 (2001) 640-648.

[31] B. Song, R.S. Amano, Application of non-linear k–ω model to a turbulent low inside a sharp U-bend, Computational Mechanics 26 (2000) 344-351.

[32] D.B. Spalding, Concentration fluctuations in a round turbulent free jet, Journal of Chemical Engineering Science 26 (1971) 95-107.

[33] X. Wang, K.F. McNamara, Evaluation of CFD simulation using RANS turbulence models for building effects on pollutant dispersion, Environmental Fluid Mechanics 6 (2006) 181-202.

[34] L.Z. Zhang, S.M. Huang, L.X. Pei, Conjugate heat and mass transfer in a cross-flow hollow fiber membrane contactor for liquid desiccant air dehumidification, International Journal of Heat and Mass Transfer 55 (2012) 8061-8072.

[35] S.M. Huang, M.L. Yang, W.F. Zhong, Y.J. Xu, Conjugate transport phenomena in a counter flow hollow fiber membrane tube bank: Effects of the fiber-to-fiber interactions, Journal of Membrane Science 442 (2013) 8-17.

[36] L.Z. Zhang, Total Heat Recovery: Heat and Moisture Recovery from Ventilation Air, Nova Sci. Pub. Co., New York, 2008.

Figure Captions

Fig.1. Schematic of the section in the cross-corrugated exchanger

Fig.2. Schematic of the experimental setup.

Fig.3. The assembled total heat exchanger with cross-corrugated triangular ducts and one-step made asymmetric membranes. (a) Half finished, with corrugated membrane plates. (b) Finished.

Fig.4. Part of the mesh structure.

Fig.5. Effect of adopted layers in the computation domain on numerical results, Re=890 (Apex angle=90°; u_m=1.327m/s).

Fig.6. Velocity contours (m/s) in the *y*-*z* plane at the center of *x* axis, Re=890 (Apex angle=90°; u_m=1.327m/s).

Fig.7. Temperature contours (K) on the *y*-*z* plane at the center of *x* axis, Re=890 (Inlet temperature of fresh air: 308K; inlet temperature of exhaust air: 300K). (a) Apex angle=60°; u_m=2.167m/s. (b) Apex angle=90°; u_m=1.327m/s.

Fig.8. Isotherms and heat fluxes on the membrane surface in the middle layer (Apex angle=90°; inlet temperature of fresh air: 308K; inlet temperature of exhaust air: 300K). (a) Temperature (K), (b) Heat flux (W/m^2).

Fig.9. Cyclic mean Nusselt numbers for each cycle along the flow, apex angle=90°, Re=890.

Fig.10. Comparison of fully developed *Nu* with Re under various boundary conditions for apex angle=60 (a) and 90 degrees (b).

Fig.11. Humidity ratio contours (kg/kg) on the *y*-*z* plane at the center of x axis, Re=890 (Inlet humidity ratio of fresh air: 0.024kg/kg; inlet humidity ratio of exhaust air side: 0.011kg/kg).

Fig.12. Humidity ratio contours (kg/kg) and mass fluxes ($kgm^{-2}s^{-1}$) on the membrane surface in the middle layer (Apex angle=90°; inlet humidity ratio of fresh air: 0.024; inlet humidity ratio of exhaust air: 0.011). (a) Humidity ratio (kg/kg), (b) Mass flux ($kgm^{-2}s^{-1}$).

Fig.13. Comparison of fully developed *Sh* with Re under various boundary conditions for apex angle=60 degrees (a) and apex angle=90 degrees (b).

Table 1. Physical properties of the membrane total heat exchanger.

Name of properties	Symbol	Unit	Value
Module dimensions	$x_F \times y_F \times z_F$	mm^3	182×182×462
Number of channels for each stream			33
Membrane thickness	δ	μm	100
Moisture diffusivity in air	D_{va}	m^2/s	2.82×10^{-5}
Pore diameter of membrane (porous part)	d_p	μm	0.45
Membrane porosity			0.75
Effective moisture diffusivity in membrane	D_{vm}	m^2/s	3.77×10^{-6}
Thermal conductivity of membrane	λ_{mem}	W/(m·K)	0.127

Table 2. Model validation with experiment data.

(a)

Test number	V_a (m^3/h)	T_{fi}(°C)	T_{ei}(°C)	T_{fo}(°C)			T_{eo}(°C)			Y_{fi}(g/kg)	Y_{ei}(g/kg)	Y_{fo}(g/kg)			Y_{eo}(g/kg)		
				Exp.	Cal.	Unc.	Exp.	Cal.	Unc.			Exp.	Cal.	Unc.	Exp.	Cal.	Unc.
1	100	35.1	27.3	32.3	31.7	±0.2	30.3	30.1	±0.2	24.92	11.73	21.80	21.13	±0.44	14.90	14.47	±0.30
2	125	35.1	27.6	32.5	31.9	±0.2	30.4	30.3	±0.2	23.87	12.22	21.26	20.76	±0.43	14.76	14.29	±0.30
3	150	35.1	26.9	32.3	31.8	±0.2	29.8	29.9	±0.2	24.66	11.34	21.90	21.82	±0.44	14.20	14.13	±0.28
4	175	34.9	27.6	32.4	32.0	±0.2	30.0	29.7	±0.2	24.34	11.64	21.80	21.77	±0.44	14.28	14.36	±0.29
5	200	35.1	26.4	32.1	32.1	±0.2	29.2	29.1	±0.2	23.98	11.05	21.55	21.31	±0.43	13.62	13.67	±0.27
6	100	25.5	15.4	21.4	21.3	±0.2	19.3	19.4	±0.2	11.02	8.35	10.34	10.31	±0.21	9.01	8.97	±0.18
7	125	25.4	15.4	21.4	21.4	±0.2	19.1	19.2	±0.2	10.75	8.17	10.14	10.12	±0.20	8.81	8.79	±0.18
8	150	25.4	15.3	21.7	21.5	±0.2	19.1	19.0	±0.2	11.06	8.77	10.50	10.46	±0.21	9.28	9.26	±0.19
9	175	25.4	15.4	21.7	21.7	±0.2	19.0	19.1	±0.2	10.77	8.77	10.33	10.31	±0.21	9.25	9.21	±0.19
10	200	25.3	16.3	22.2	21.9	±0.2	19.6	19.4	±0.2	11.22	9.32	10.79	10.76	±0.22	9.75	9.70	±0.20

(b)

Test number	ε_s(%)			ε_L(%)			f		
	Exp.	Cal.	Unc.	Exp.	Cal.	Unc.	Exp.	Cal.	Unc.
1	37.18	39.74	±1.56	23.84	24.75	±1.60	0.323	0.319	±0.030
2	36.00	39.33	±1.51	22.10	22.23	±1.48	0.303	0.281	±0.028
3	34.76	38.41	±1.46	21.10	21.13	±1.41	0.273	0.254	±0.025
4	33.56	34.25	±1.41	20.39	20.83	±1.37	0.260	0.232	±0.024
5	33.33	32.76	±1.40	19.33	20.46	±1.30	0.237	0.216	±0.022
6	39.60	40.59	±1.66	25.09	24.91	±1.68	0.328	0.319	±0.030
7	38.50	39.00	±1.62	24.22	24.22	±1.62	0.290	0.281	±0.027
8	37.13	37.62	±1.56	23.36	23.8	±1.57	0.266	0.254	±0.024
9	36.50	37.00	±1.53	23.00	22.5	±1.54	0.250	0.232	±0.023
10	35.56	36.11	±1.49	22.63	22.11	±1.52	0.233	0.216	±0.021

Table 3. Performance comparisons of total heat exchangers with different structures and membrane types under the same air flow rates V_a=150 m^3/h.

Properties		Structures		
		Parallel-plate	Plate-fin	Cross-corrugated
Channel dimension(mm)		462×185×185	462×185×185	462×185×185
Channel height, H (mm)		2	5	2.8
Channel width, W (mm)		58	10	5.6
Number of flow channels		230	95	162
A_{tot} (m^2)		7.9	7.9	7.9
Inlet air velocity (m/s)		0.975	0.975	1.950
Re		261	345	532
f		0.368	0.130	0.503
ΔP (Pa)		10	3	53
Nu		5.60	1.35	10.44
h_f,h_e (W m^{-2} K^{-1})		34.3	6.3	63.2
ε_s		0.75	0.55	0.86
Composite	*Sh*	3.16	0.74	6.04
membrane	k_f, k_e (m/s)	0.023	0.004	0.043
	ε_L	0.63	0.30	0.73
Asymmetri	*Sh*	5.41	1.26	10.32
c	k_f, k_e (m/s)	0.039	0.007	0.073
membrane	ε_L	0.72	0.39	0.81

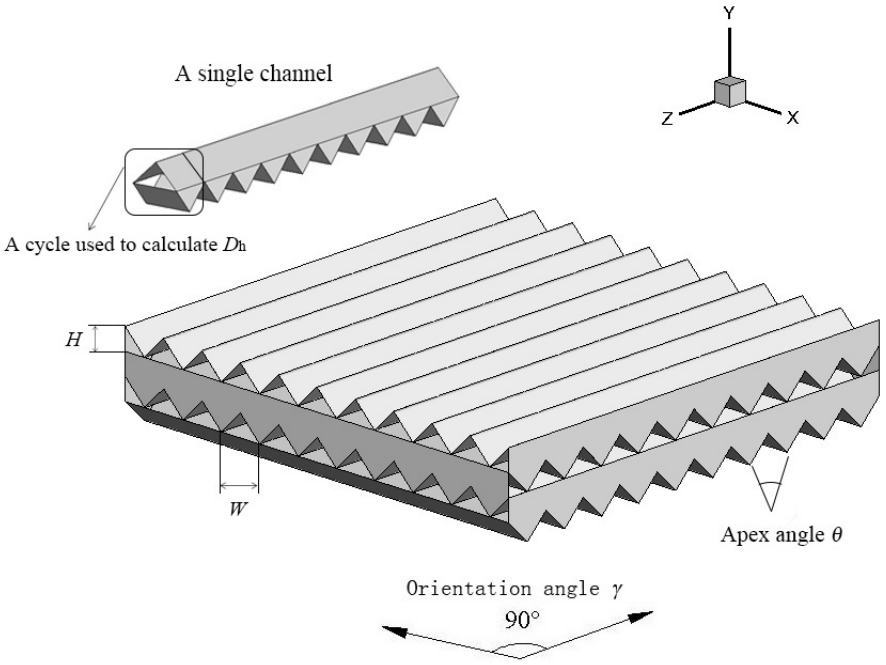

Fig.1. Schematic of a cross-corrugated triangular duct heat and mass exchanger.

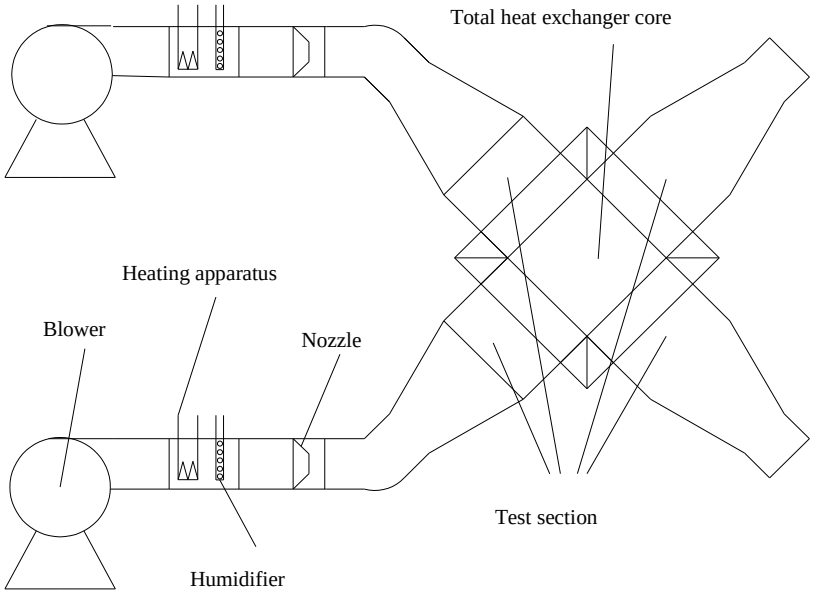

Fig.2. Schematic of the experimental setup.

(a) Half finished, with corrugated membrane plates.

(b) Finished.

Fig.3. The assembled total heat exchanger with cross-corrugated triangular ducts and one-step made asymmetric membranes. (a) Half finished, with corrugated membrane plates. (b) Finished.

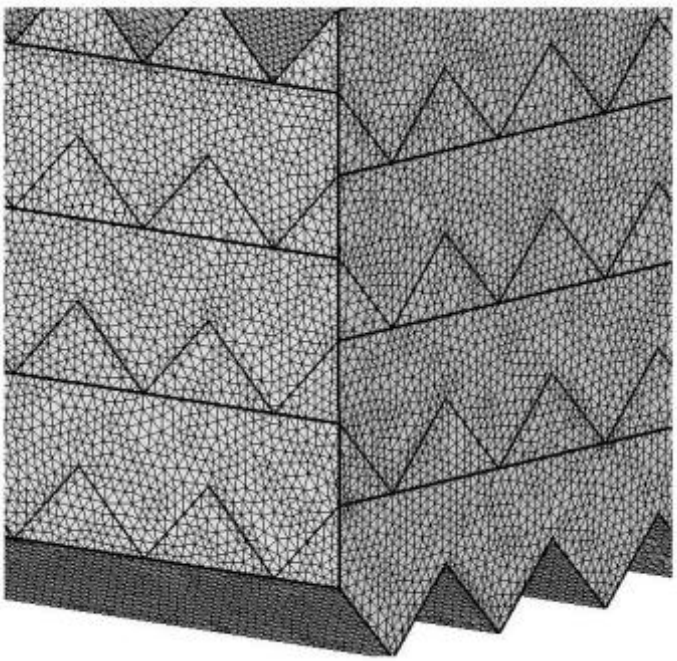

Fig.4. Part of the mesh structure.

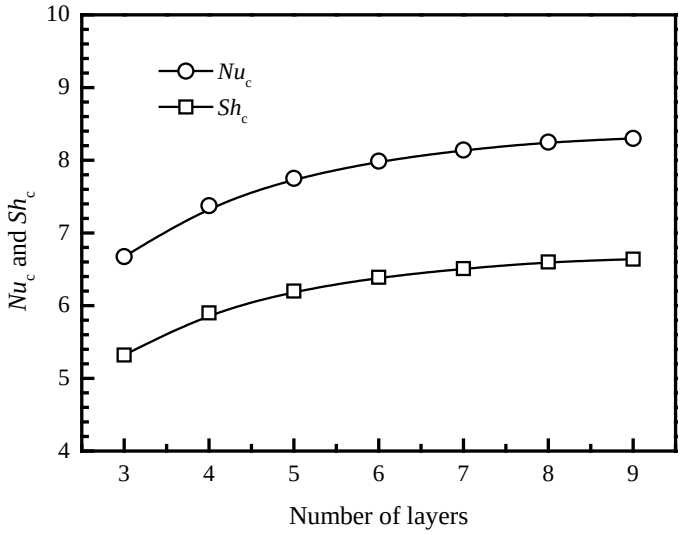

Fig.5. Effect of adopted layers in the computation domain on numerical results, Re=890 (Apex angle=90°; u_m=1.327m/s).

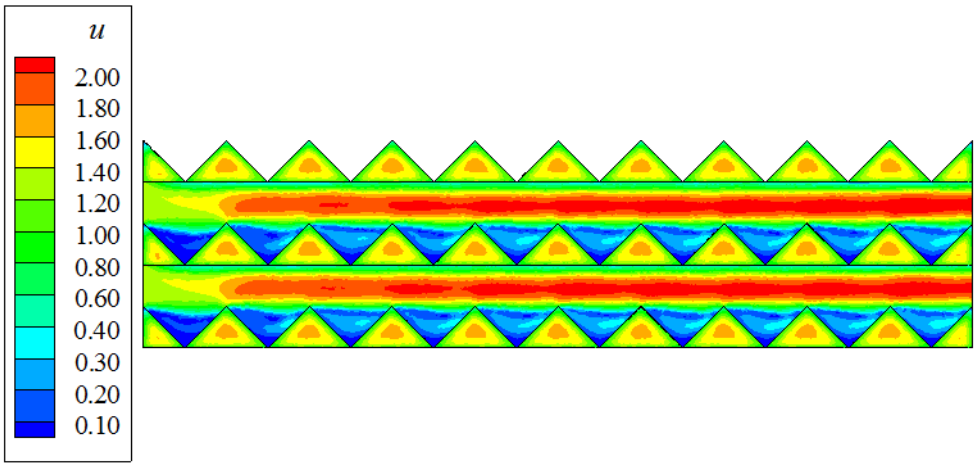

Fig.6. Velocity contours (m/s) in the *y*-*z* plane at the center of *x* axis, Re=890 (Apex angle=90°; u_m=1.327m/s).

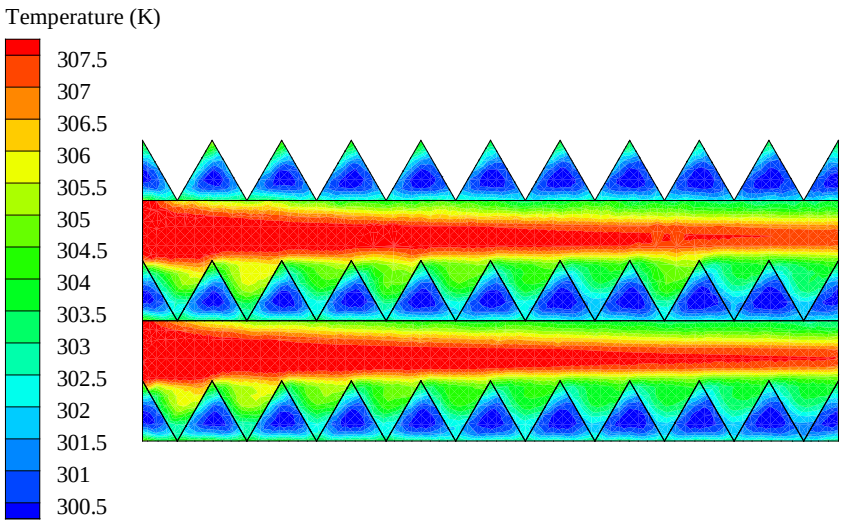

(a) Apex angle=60°; u_m=2.167m/s

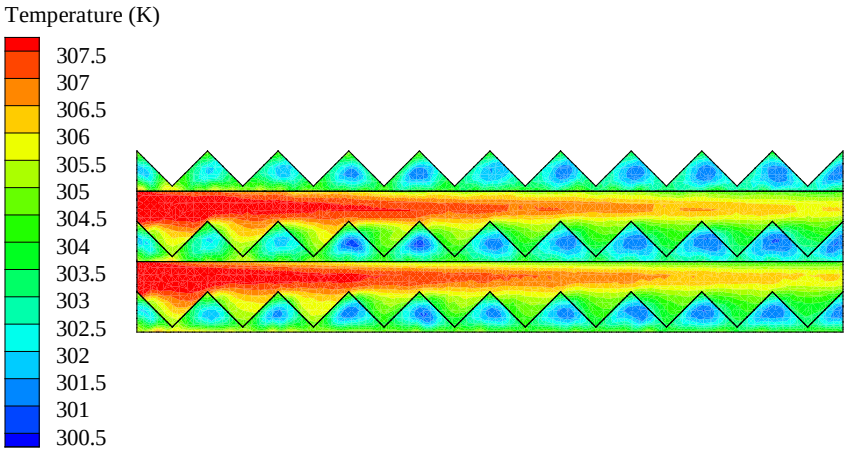

(b) Apex angle=90°; u_m=1.327m/s

Fig.7. Temperature contours (K) on the *y*-*z* plane at the center of *x* axis, Re=890 (Inlet temperature of fresh air: 308K; inlet temperature of exhaust air: 300K).

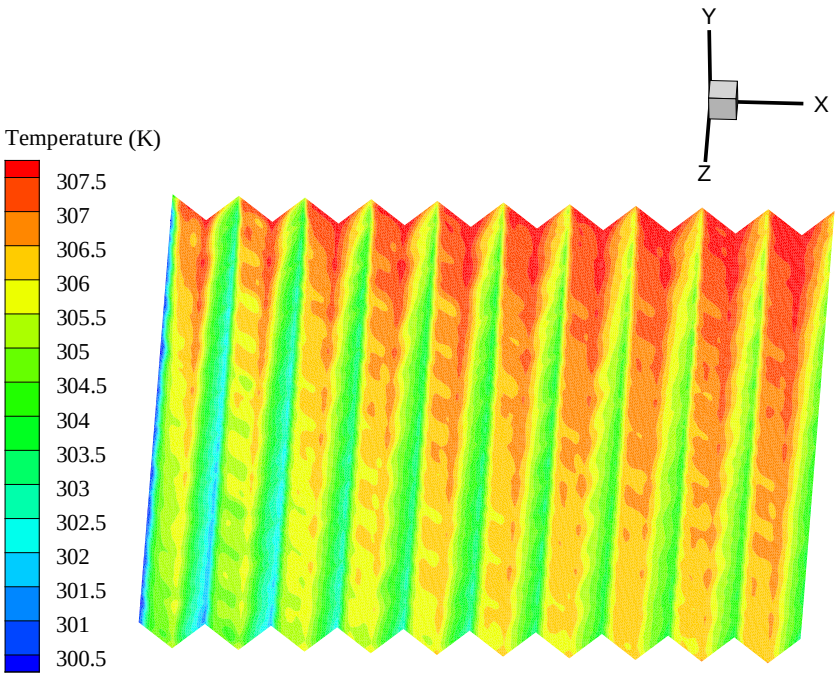

(a) Temperature (K)

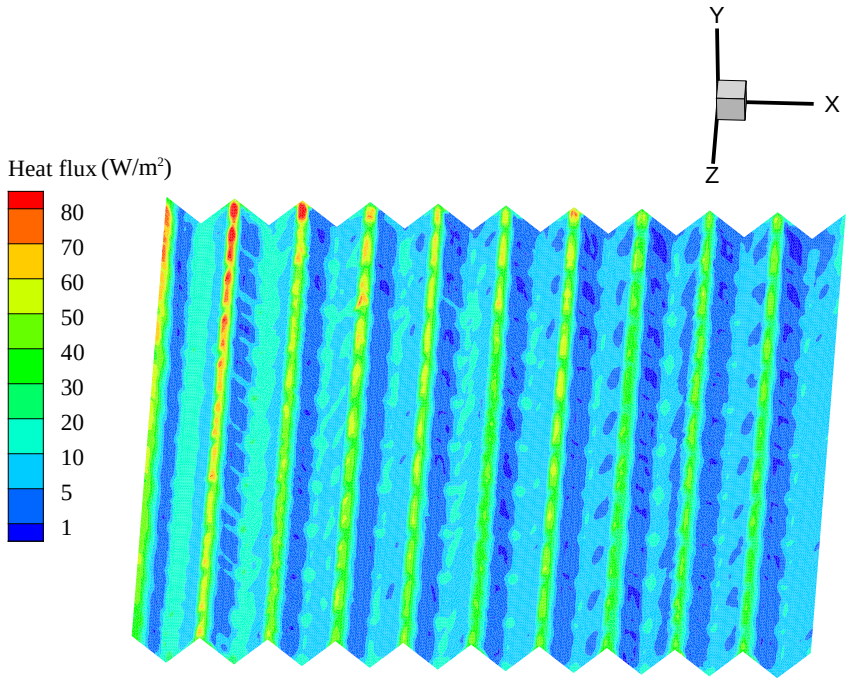

(b) Heat flux (W/m^2)

Fig.8. Isotherms and heat fluxes on the membrane surface in the middle layer (Apex angle=90°; inlet temperature of fresh air: 308K; inlet temperature of exhaust air: 300K). (a) Temperature (K), (b) Heat flux (W/m^2).

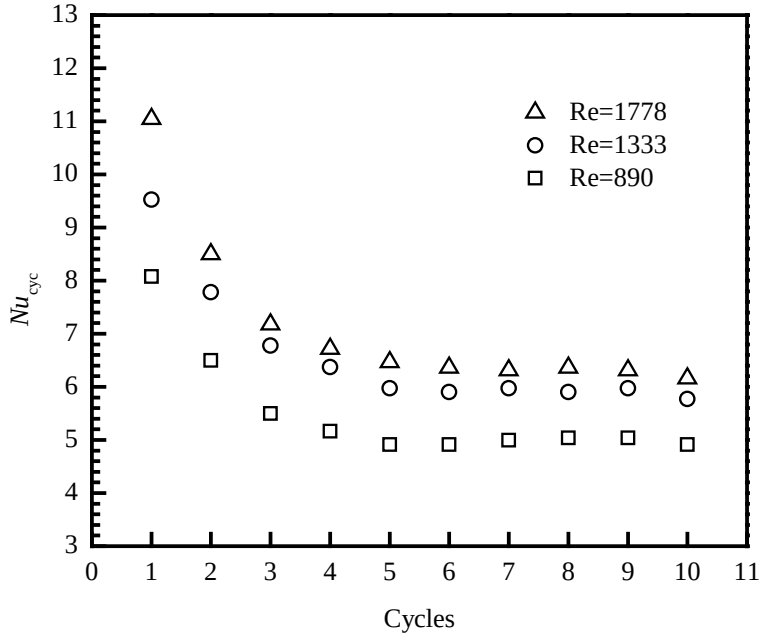

Fig.9. Cyclic mean Nusselt numbers for each cycle along the flow, apex angle=90°, Re=890.

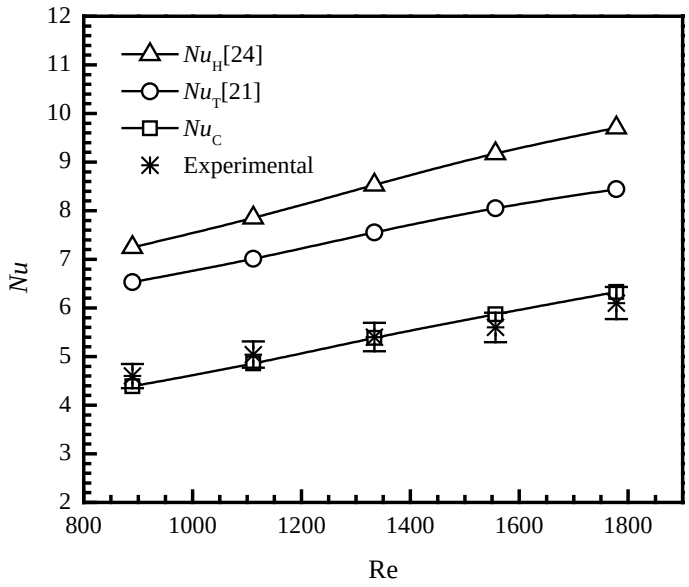

(a) Apex angle=60°

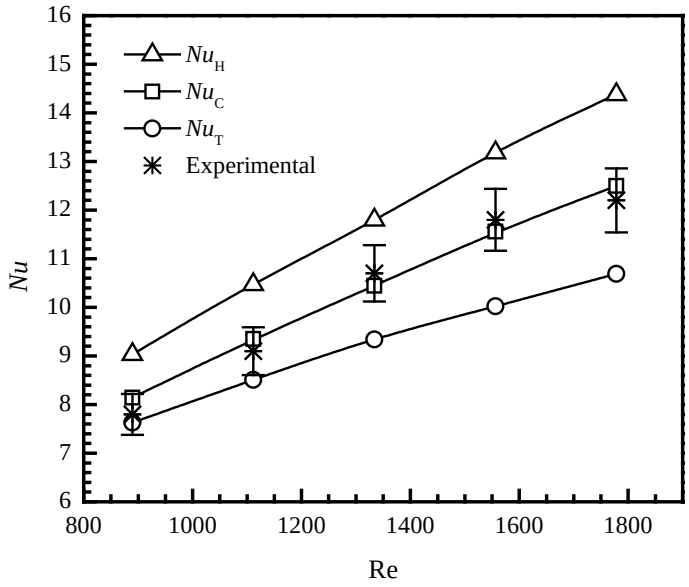

(b) Apex angle=90°

Fig.10. Comparison of fully developed *Nu* with Re under various boundary conditions for apex angle=60 (a) and 90 degrees (b).

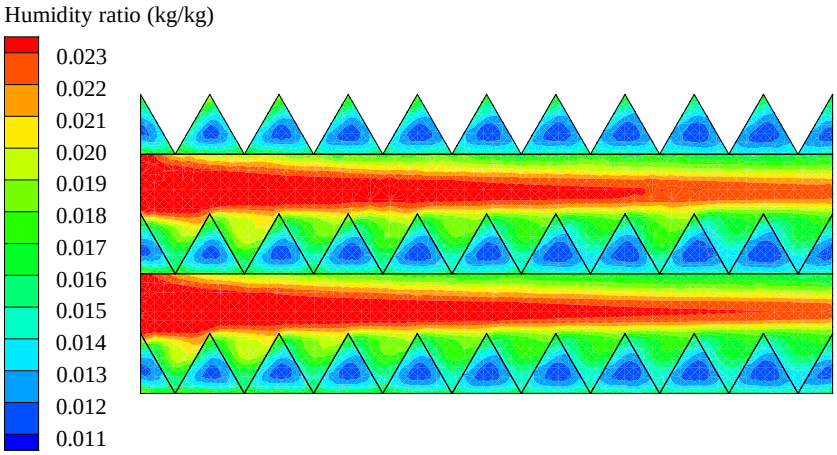

(a) Apex angle=60°; u_m=2.167m/s

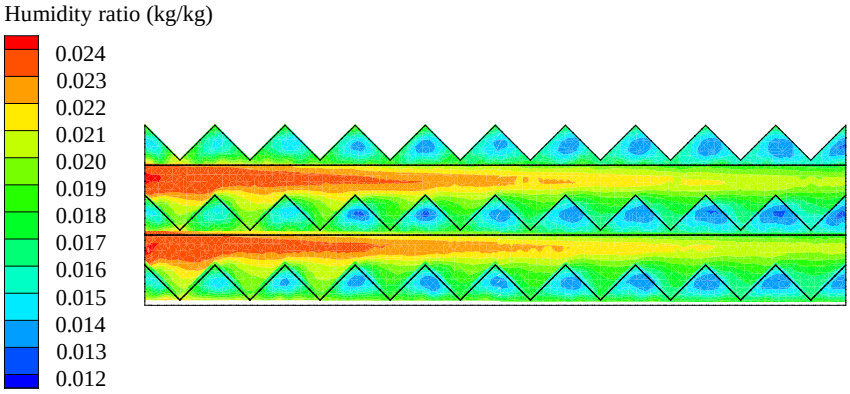

(b) Apex angle=90°; u_m=1.327m/s

Fig.11. Humidity ratio contours (kg/kg) on the *y-z* plane at the center of *x* axis, Re=890 (Inlet humidity ratio of fresh air: 0.024kg/kg; inlet humidity ratio of exhaust air side: 0.011kg/kg).

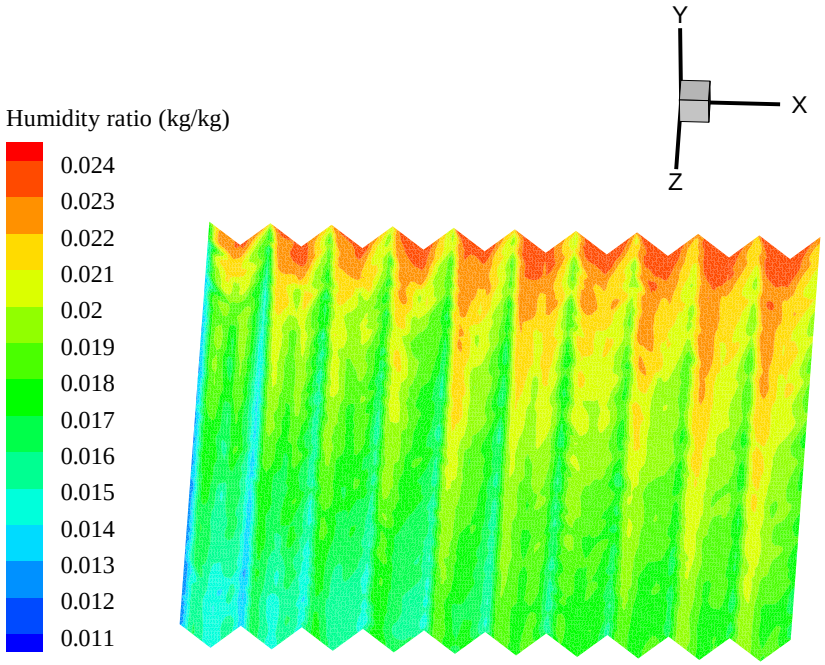

(a) Humidity ratio (kg/kg)

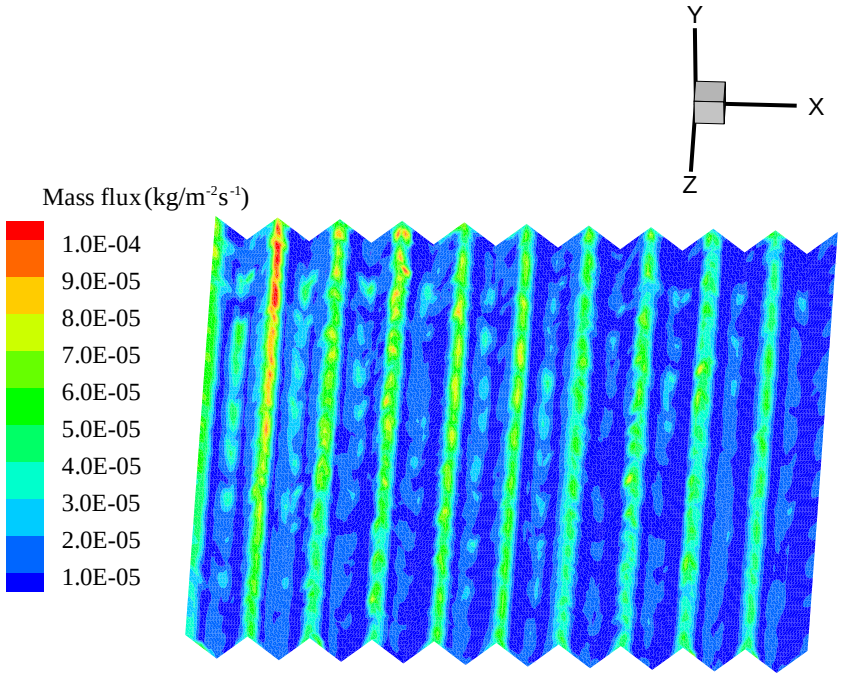

(b) Mass flux ($kgm^{-2}s^{-1}$)

Fig.12. Humidity ratio contours (kg/kg) and mass fluxes ($kgm^{-2}s^{-1}$) on the membrane surface in the middle layer (Apex angle=90°; inlet humidity ratio of fresh air: 0.024; inlet humidity ratio of exhaust air: 0.011). (a) Humidity ratio (kg/kg), (b) Mass flux ($kgm^{-2}s^{-1}$).

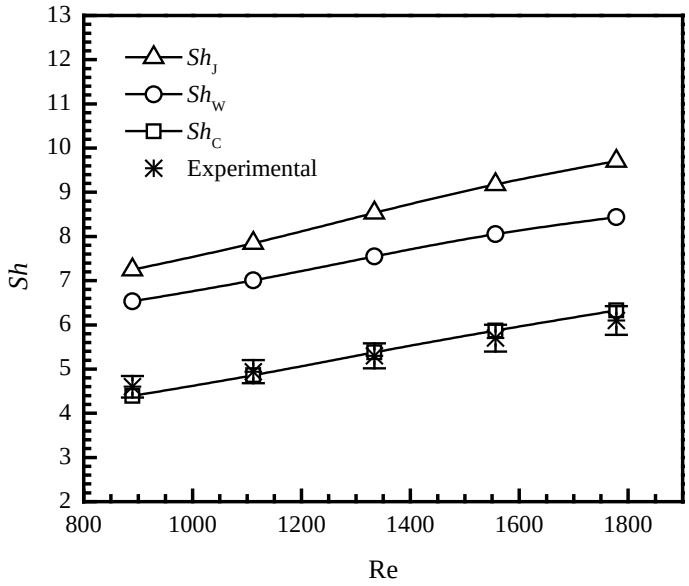

(a) Apex angle=60°

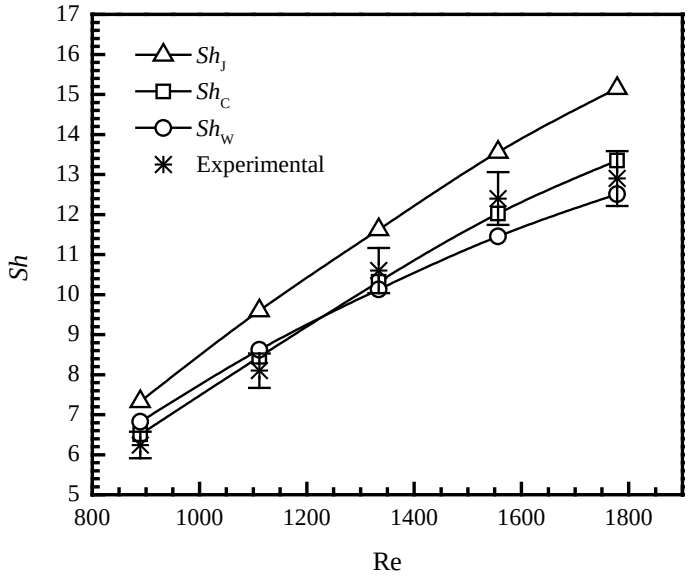

(b) Apex angle=90°

Fig.13. Comparison of fully developed *Sh* with Re under various boundary conditions for apex angle=60 degrees (a) and apex angle=90 degrees (b).